ChemElectroChem

Research Article
doi.org/10.1002/celc.202201130

Chemistry Europe
European Chemical Societies Publishing

www.chemelectrochem.org

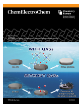

Electrochemical Cycling Behaviour and Shape Changes of Zn Electrodes in Mildly Acidic Aqueous Electrolytes Containing Quaternary Ammonium Salts

Benedetto Bozzini,*[a] Marco Boniardi,[b] Tommaso Caielli,[a] Andrea Casaroli,[b] Elisa Emanuele,[a] Lucia Mancini,[c, d] Nicola Sodini,[d] and Jacopo Strada[a]

Secondary Zn–based batteries are a valid alternative to Li for stationary storage, but commercial devices are not yet available, chiefly owing to anode shape-change and passivation issues. Mildly acidic aqueous solutions are actively studied, since they seem to limit unstable growth of Zn, with respect to the alkaline ones, customary for primary batteries. Additives can further improve the performance of mildly acidic electrolytes. In this work we focus on the impact of a series of quaternary ammonium salts (TBAB, CTAB, DMDTDAB, BDMPAC, BPPEI, PDADMAC), selected to represent a comprehensive range of molecular functionalities. Electrochemical measurements (cyclic voltammetry, chronopotentiometry and galvanostatic-cycling in split-cells), combined with 2D and 3D imaging techniques (SEM, stereomicroscopy and *in situ* tomography) were adopted for the assessment Zn behaviour. This multi-technique approach pinpointed TBAB as the single most effective additive for low-current density operation, while at high current densities the additive-free electrolyte allows better cycling performance, coherently with similar results for alkaline electrolytes.

Introduction

The electrification of the mobility sector and the necessity to store electrical energy from renewable sources have increased the global demand for rechargeable batteries.[1–3] However, there are many drawbacks of the technologies currently adopted for these scopes. Lithium ions batteries are now the standard technology in use on electric vehicles, due to their outstanding performances in terms of low weight and high power density.[4–6] The cost of Li-ion batteries is although high, due to the complex manufacturing process and the expensive materials. Moreover, there are serious concerns about the long-term availability, the geo-political distribution, and the impact on the environment related to Lithium and Cobalt. Li-ion batteries also have major safety problems, due to the flammability of the organic electrolyte.[7,8] The other main type of accumulators on the market is the lead-acid battery, a well-understood technology, but suitable only for stationary applications due to the high weight, and with some concern about the toxicity of lead.[9,10] A secondary battery based on Zn would have many advantages and could solve the above-mentioned critical issues.[11] Zn metal is slightly more abundant than lithium, but, most importantly, it is more evenly geo-politically distributed and has a broad range of low-cost widespread and consolidated applications. It is non-toxic, and it is possible to produce batteries with an aqueous electrolyte, which makes them intrinsically safe and environmentally friendly. Zn is a material adopted for battery anodes since the invention of the battery itself, anyway the development of a rechargeable device based on Zn must face many technological challenges, which have impeded the commercialization of Zn-based rechargeable batteries to these days. Today there are five main device concepts for the rechargeable Zn battery; the Zn–air secondary battery, the Zn-ion battery, the rechargeable Zn-alkaline battery, the Zn–Ni battery[12,13] and hybrid batteries with a Zn anode and a Li-ion intercalation cathode.[14–18] A key obstacle to the production of Zn-ion batteries is the poor cyclability of the Zn metal, which typically leads to a rapid performance drop or battery failure.[19] In a metallic negative electrode, the metal oxidizes, and generally dissolves, during discharge and electrodeposits during charge. Non-compact deposit structures are a major issue for the cyclability of Zn-based batteries, indeed dendrites and mossy aggregates can grow through the electrolyte separator and reach the cathode, short-circuiting the battery and causing an immediate failure, moreover non-compact Zn structures are brittle, they tend to break, disconnect electrically from the anode, and be oxidized under free corrosion in the electrolyte, which is detrimental because it

---

[a] *Prof. B. Bozzini, T. Caielli, E. Emanuele, J. Strada*
Department of Energy
Politecnico di Milano
via Lambruschini 4, 20156 Milano (Italy)
E-mail: benedetto.bozzini@polimi.it

[b] *Prof. M. Boniardi, Dr. A. Casaroli*
Department of Mechanical Engineering
Politecnico di Milano
via la Masa 1, 20156 Milano (Italy)

[c] *Dr. L. Mancini*
Slovenian National Building and Civil Engineering Institute (ZAG)
Dimičeva ulica 12, SI-1000 1000 Ljubljana (Slovenia)

[d] *Dr. L. Mancini, N. Sodini*
Elettra – Sincrotrone Trieste S.C.p.A.
S.S. 14–km 163.5 in Area Science Park, 34149, Basovizza, Trieste (Italy)

Supporting information for this article is available on the WWW under https://doi.org/10.1002/celc.202201130

favours the accumulation of oxides close to the anode and mainly because it causes a loss of anode material. This decreases the battery capacity and mandates to oversize the mass of Zn in the anode, to compensate these losses. Passivation and corrosion of the Zn anode are also serious problems, leading to other common modes of battery failure, such as the development of high internal resistances and capacity fade. Moreover, the space distribution of passivation has a bearing on anode performance, since uneven passivation, which insulates only some portions of the electrode surface, causes a heterogeneous current density c.d., which leads to the formation of pits during discharge and favours the formation of non-compact structures during charge. The literature relevant for this topic was examined in detail and a critical account in brief is offered in Section S1 of the Supporting Information. In recent times, many studies were made concerning secondary battery application, these generally focus on the engineering and performances of materials,[11,20] but a very limited number of fundamental studies were found on the behaviour of Zn under the alternation of anodic and cathodic polarization conditions:[21–23] it is extremely complicated to describe and model univocally this process due to the wide range of parameters involved. This work concentrates on the analysis of the link between electrochemical behaviour upon cathodic/anodic cycling and the morphology evolution – as followed by *post mortem* and *in situ* and micro-imaging – of Zn, in the form of foils, in mildly acidic aqueous electrolytes-the system of choice in ZIB present-day battery research-, that is also starting to be considered for Zn-air batteries – without and with addition of organic additives, quaternary ammonium salts (QASs), in particular.

Problems related to deposits morphologies are more pronounced in alkaline environment, where non-compact structures have a higher tendency to grow. This is one key reason for the increasing interest in alterative water-based electrolytes, among which mildly acidic (in battery chemistries such as zinc-ion battaries (ZIB),[24,25] rechargeable zinc-air batteries[26–29] and hybrid batteries with a Zn anode and a Li-ion intercalation cathode[16,17]) and highly-concentrated[30,31] electrolytes: the focus of this work will be on the former approach. It is worth noting that the formation of mossy zinc occurs at lower c.d.s than compact deposits, so that the c.d. working range during charge which allows to have a high cyclability, has not only an upper limit due to dendritic growth but also a lower one, since Zn anodes might have problems also working at low c.d.s: it is worth stressing that the literature on Zn anodes did not address this issue, to date.

The ideal additive must prevent the formation of non-compact structures, suppress corrosion, and avoid passivation, without reducing excessively the reaction kinetics. Differently from the additives proposed for electrodeposit levelling and corrosion inhibition, battery additives must work during both anodic and cathodic polarization cycles. The additive effects in a condition different from the nominally sought after one (cathodic polarization for levellers and anodic polarization for corrosion inhibitors) are not investigated in the existing literature, apart from seminal work in alkaline ambient.[21,23] From this paper it will appear clearly that mossy Zn formation is probably the single most critical unstable growth mode during recharge of Zn anodes in the c.d. range of practical interest. Thus, if an additive guarantees an effective suppression of high-c.d. dendrites, it does not necessarily suppress also mossy structures formation and vice versa.

Results and Discussion

This study is aimed at assessing the impact of the QASs, belonging to the series presented in the Materials Subsection of the Experimental Section, on the shape changes of Zn, resulting jointly from the application of cathodic and anodic polarization in mildly acidic $ZnSO_4$ solution, that is typical of battery cycling This series has been selected in order to express a comprehensive variety of the functionalities linked to the quaternary ammonium cation. The specific rationale for the choice of the individual QASs is provided below. (i) Hexadecyl (or cetyl) tri-methyl ammonium (as bromide salt: CTAB) is a quaternary ammonium (QA) cation with a single, long aliphatic chain; (ii) tetra n-butyl ammonium (as bromide salt: TBAB) is a QA cation with four short aliphatic chains; (iii) di-methyl di-tetradecyl ammonium (as bromide salt: DMDTAB) is a QA cation with two long aliphatic chains; (iv) benzyl dimethyl phenyl ammonium (as chloride salt: BDMPAC) is a QA with aromatic functionalities; (v) benzyl-phenyl modified polyethyleneimine (in chloride form: BPPEI) is a polymer with QA sites and the same aromatic moieties as BDMPAC; (vi) poly di-allyl di-methyl ammonium (as chloride salt: PDADMAC): is polymer with cyclic QA functionalities. Use of the QASs we selected for this work for Zn dendrite suppression is documented: CTAB[21,32–34] and the molecularly similar trimethyloctadecylammonium chloride (STAC);[35] TBAB;[21,32,36] polyethyleneimine (PEI)[37] moreover, PEI with aromatic QA moieties (BPPEI) was employed in the electrodeposition of Zn from alkaline solutions in[21] and in acidic Cu baths.[38] The effect of BDMPAC on the electrodeposition of Zn and Au was studied in[21] and,[39,40] respectively. Lastly, PDADMAC has been studies as an additive for alkaline Zn in,[21] where it was shown to form cathodic films exhibiting single-ion conducting properties.[41]

The tools employed in this research are combined cathodic-anodic electrochemical measurements (Subsection on Galvanostatic cycling of coin cells in the Results and Discussion Section) and imaging on the different lengthscales that are relevant to electrochemical phase formation (Subsection on Imaging analysis of Zn electrode shape changes Galvanostatic in the Results and Discussion Section).

Cyclic voltammetry (CV)

CV measurements have been carried out, encompassing the cathodic and anodic potential ranges – to assess the impact on the electrochemical response, of having previously polarized the Zn electrode in the previous one, thus following the special types of electrokinetic irreversibilities related to c.d. switching.

Morevover, cycling has been continued for 10 cycles, in order to assess the build-up of the mentioned irreversibility.

The CV behaviour in the additive-free electrolyte has been the object of a dedicated study,[22] the key outcomes of which will be briefly summarized here for the readers' perusal, and this will be used as the reference condition on the background of which the effect of the different QASs has been analysed.

The CV pattern obtained with a GC electrode in contact with the additive-free $ZnSO_4$ electrolyte is reported in black in all panels of Figures 1 and 2, and is characterized by the following key features. First of all, we would like to stress that three independent repetitions of all the data shown in these figures have been measured (see also Subsection Cyclic voltammetry of the Experimental Section), and that the results of these replicates are in excellent quantitative matching, with a well-defined and controlled deviation of the current values, which was always below 15%.

Electrodeposition of Zn starts at ca. -1.15 V in the first cycle, where Zn nucleates onto bare glassy-carbon, and at ca. -1.10 V in the subsequent cycles, in which Zn nucleates in the presence of a film or residual corrosion products. After an initial Butler-Volmer type c.d. growth, the mass-transport controlled peak forms, showing a maximum at ca. -1.17 V. Limiting c.d. conditions are reached during the return scan, as one can notice from the plateau in the range $-1.5 \div -1.3$ V. At high cathodic potentials, close to -1.5 V, an additional peak is found, compatible with the reduction of zinc hydroxides and basic salts, forming in the catholyte owing to alkalinization by parasitic HER. The c.d. in the cathodic loop decreases upon cycling: this type of electrochemical response has been observed in[22] for the case of an additive-free electrolyte of the same type, and explained-on the basis of soft-X ray absorption microspectroscopy – with the accumulation of corrosion products that can neither be fully solubilized in the anodic interval, nor totally reduced in the cathodic branch. We think that the same explanation can be extended to the case of additive-containing mildly acidic electrolytes.

The anodic behaviour is dominated by the stripping of Zn deposited in the cathodic branch, and exhibits an evident peak, followed by a relatively sharp decrease, terminating with a low-c.d. tail extending for some tens of mV. Notwithstanding the fact that active corrosion is the dominating process in the relevant electrolyte, the residual c.d. tail can be justified with the formation of a pseudo-passivating Zn(II)-containing film, impeding the completion of Zn stripping, coherently with the progressive c.d. observed in the cathodic loop and continued in the anodic branch. From the mechanistic viewpoint, this process is compatible with the formation of type II oxides under anodic conditions, and with the precipitation of zinc basic salts in the cathodic branch. Of course, both processes can decrease the active electrodic area and can also lead to the formation of a porous layer of type-I oxide, also hindering mass transport.

Combining CV and XAS mapping, in,[22] we evidenced that these cycle-dependent voltammetric patterns are controlled by parasitic phase formation in the build-up of locally passivating layers, that trigger shape changes. In fact, the formation of zincates due to alkalinization of the catholyte, followed by their precipitation resulting from cathodic supersaturation and dehydration to ZnO, generates complex morpho-chemical patterns on the Zn electrode, with patches of different ionic and electronic conductivity. These heterogeneities at the

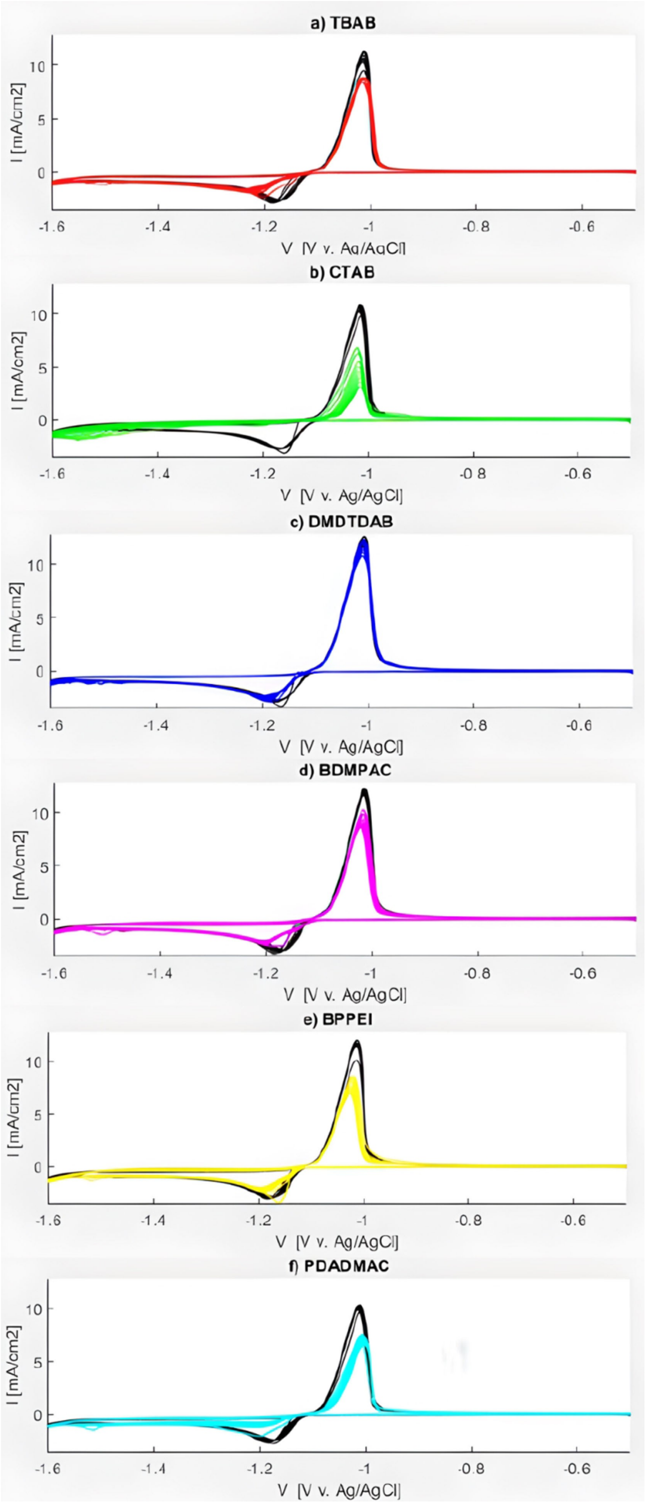

Figure 1. Cyclic voltammograms (CVs) recorded with a glassy carbon electrode in contact with a 0.5 M Na_2SO_4 + 10 mM $ZnSO_4$ aqueous solution, without (black plots) and with the indicated QAS additives. Number of cycles: 10: sequential scans converge to a limiting cycle. Scan rate 25 mV s^{-1}.

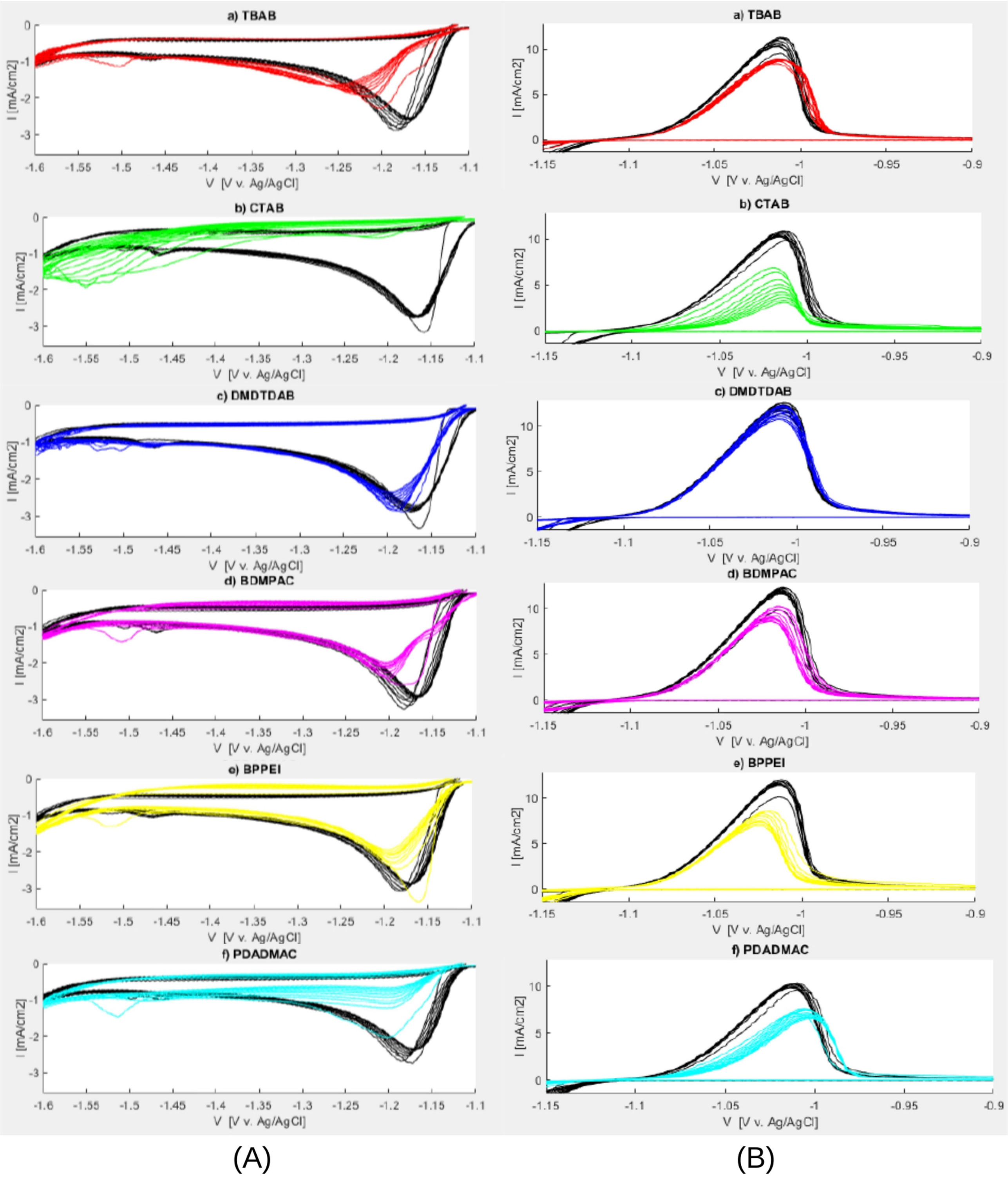

Figure 2. Same curves of Figure 1, highlighting separately the: (A) cathodic and (B) anodic branches.

mesoscale, developing at the electrode surface, control the local c.d. distribution, that is responsible for nucleation distribution of new phases and the local deactivation of the electrode, finally leading to mossy or dendritic growth in selected regions.

In Figure 1 we report the CV measured in the presence of the selected QAS and in Figure 2 we re-propose the same curves, highlighting separately the anodic and cathodic regions. For a more insightful comparison of electrochemical behaviour of Zn in the different electrolytes considered, we computed some quantities that are characteristic of the electrodic processes going on in the cathodic and anodic branches, as a function of the progress of cycling. In Figure 3 we report: the maximum c.d. at the cathodic and anodic peaks (Panels (a) and (b)) and the charge consumed in the cathodic and anodic processes (Panels (c) and (d)), in the presence and in the absence of additives.

Addition of TBAB (red plots in Figures 1–3) causes the development of two cathodic Tafel-type slopes, both of which are drastically lower than in the additive-free system. In addition, also the mass-transport controlled cathodic peak and the cathodic exchanged charge are lowered and, in addition, they tend to decrease with cycling, while the cathodic limiting c.d. is not measurably affected. The anodic Tafel-type slope, peak position and consumed charge are slightly decreased, and their evolution with cycling, is not appreciably affected by the presence of the additive. This behaviour shows that the chief effect of the additive is mainly on the nature of the cathodic process, with a slight anodic inhibiting effect.

CTAB addition brings about a notable cathodic and anodic inhibition (green plots in Figures 1–3), that increases with cycling. The evolution of the cathodic feature at high c.d.s, that we have explained with the precipitation of basic salts,[22] is strongly evidenced with this additive, denoting a relatively more significant effect of catholyte alkalinisation in this system.

DMDTDAB (blue plots in Figures 1–3) addition is associated with only slight modifications of the CV behaviour, essentially resulting in an increase of the nucleation overvoltage, that is not modified upon cycling, a limited degree of cathodic inhibition and a hardly appreciable anodic effect.

BDMPAC (purple plots in Figures 1–3) additive exhibits a voltammetric response that is similar to that of TBAB – including the presence of a double cathodic Tafel-type slope-, with slightly weaker cathodic inhibition and moderately stronger anodic suppression.

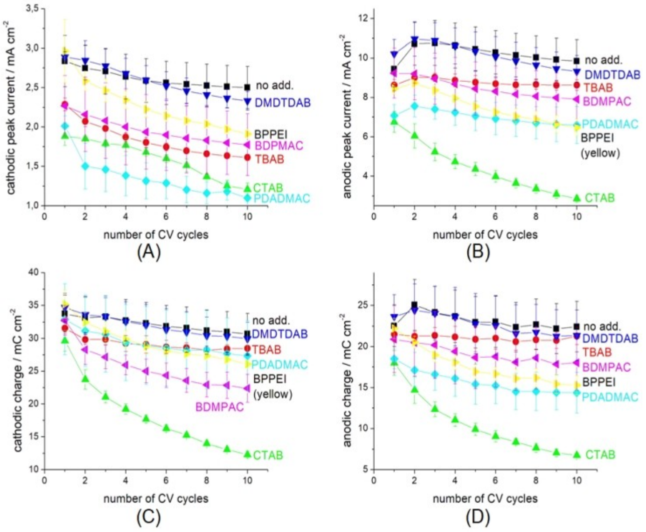

Figure 3. Characteristic electrochemical quantities, derived from CVs of Figure 1: the different electrolytes are addressed with the colour codes given in Figure 1.

BPPEI (yellow plots in Figures 1–3) shows the lowest degree of cathodic inhibition among the investigates additives in the Tafel-type and mass-transport controlled regimes, while it shows a marked depression of the limiting c.d., accompanied by a sizable progressive decrease of the cathodic c.d. upon cycling: the formation of a ionomeric film at the cathode surface, highlighted in aqueous alkaline solutions[21] could explain this behaviour. The anodic branch is quite similar to that of BDMPAC, that contains the same moieties, though in a polymeric network, with a slightly higher inhibiting action.

Similarly to CTAB, but with differences in quantitative details, PDADMAC (light blue plots in Figures 1–3) brings about a notable cathodic inhibiting effect, but, at variance with CTAB, the progressive nature of the inhibition is far less marked and most of the inhibiting effect seems to develop after the first cycle. In the anodic range, stable and relatively strong inhibition is found.

The inhibition of the deposition reaction brought about by the investigated additives, can be associated to two effects: (i) the kinetic inhibition of the deposition reaction, a purely cathodic effect, and (ii) the formation of a layer of oxides and/or reacted additives, which reduce the active area: a process which is influenced both by cathodic (alkalinization by HER or reduction reactions/irreversible adsorption of additives) and anodic behaviour (oxides formation). A convenient way to convey the information gleaned from the corpus of voltammetric data in a synthetic way, is a ranking of the investigated QASs on the basis of their impact on voltammetric descriptors addressing the two above-mentioned effects. Thus, the following observables are adopted to establish a ranking of the additives.

(i) reduction of the cathodic Tafel slope in the first cycle, denoting kinetic inhibition of electrodeposition reaction, according to which we obtain the ranking:

$$\begin{aligned}&\text{CTAB} > \text{PDADMAC} > \text{TBAB} > \text{BDMPAC} > \text{BPPEI} > \text{DMDTDAB}\\&\cong \text{no additive}\end{aligned} \tag{1}$$

(ii) Progressive reduction of cathodic currents with cycling and low ratio of the charges exchanged between the anodic and cathodic processes, indicating increased passivation by cathodic and anodic layer formation and globally denoting passivation. With this criterion the following ranking results:

$$\begin{aligned}&\text{CTAB} > \text{PDADMAC} > \text{BPPEI} > \text{TBAB}\\&\cong \text{BDMPAC} > \text{DMDTDAB} > \text{no additive}\end{aligned} \tag{2}$$

A correspondence can be established between electrodeposition inhibition and cathodic/anodic layer formation on the one hand, and adsorption/desorption rates of the additive molecule on the Zn electrode. Strong adsorption/slow desorption of the additive, in combination with modification of the corrosion products film, such as organic/ZnO composite formation, modification of the I-/II-ZnO ratio, tuning of the doping of I-ZnO. Of course, this conjecture will require explicit testing by XAS microspectroscopy as proposed in our seminal paper.[22]

On the basis of this simple mechanistic explanation, combining the electrodeposition and passivation inhibition rankings by averaging the ordering of the entries in Eqs. (1) and (2), a joint inhibition index (JII) can be proposed, that in the present case is represented in Figure 4. It can be noticed that, on the one hand DMDTDAB and, on the other hand, PDADMAC and CTAB, afford individually the weakest and strongest electrodeposition and passivation inhibition, respectively. Instead, BDMPAC, BPPEI and TBAB exhibit different degrees of individual electrodeposition and passivation inhibition and lie in the range of intermediate JII values. In the rest of this research, we shall find that this index is useful to rationalize morphological effects of the QASs investigated.

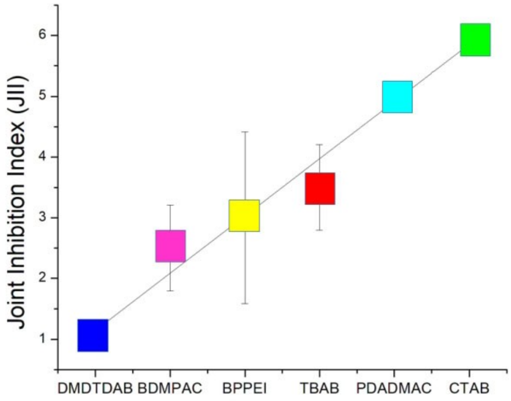

Figure 4. The Joint Inhibition Index, derived from analysis of the CVs of Figure 1, describing the combined inhibiting effect of the QASs investigated on electrodeposition and passivation.

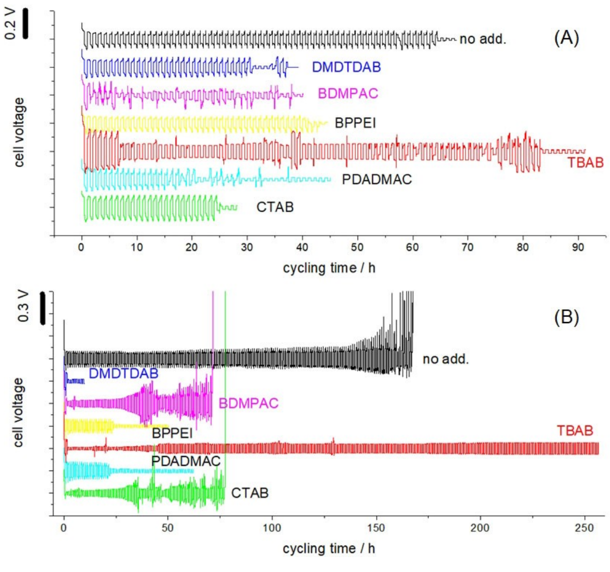

Figure 5. Cell-potential time series for symmetric Zn|Zn CR2032 coin cells with aqueous 2 M $ZnSO_4$ without and with the indicated QAS additives. Galvanostatic anodic/cathodic cycles of 1 h: (A) 1 and (B) 10 mA cm^{-2}.

Galvanostatic cycling of coin cells

Symmetric CR2032 coin cells with two Zn electrodes were built (as detailed in Subsection Galvanostatic charge/discharge cycles of the Experimental Section), with 2 M $ZnSO_4$ electrolyte without and with addition of the six QASs tested in the Cyclic voltammetry Subsection of the Results and Discussion Section. In Figure 5 we show one of the two replicated cycling experiments carried out at 1 and 10 mA cm^{-2}: all the replicated are reported in Figures S7–S13 of the Supporting Information. In Figure 6 we summarise the key outcomes of the cycling experiments, expressed in terms of the time-to-failure of the cells: the information is organized with the additives arranged along the abscissa in the order of the JII. As described in,[23] it is possible to extract richer information from the cell potential time series, employing an electrocrystallization model, that allows to assign metal growth, passivation and mass-transport parameters by comparing the experimental and computed potential responses to galvanostatic cycing: this analysis is beyond the scope of the present paper and the simple, traditional time-of-failure information is enough to assess the impact of the investigated additives.

From Figures 5 and 6 it can be noticed that galvanostatic cycling at these two c.d.s, of practical interest[42] and corresponding to the mossy-growth range (see Imaging analysis of Zn electrode shape change Subsection of the Results and Discussion Section) is strongly impacted by the nature of the QAS, both positively and negatively with respect to the additive-free case. In all cases it can be noticed that, with the exception of DMDTDAB, cycling at the higher c.d. results in delayed failure. Moreover, all systems fail by short-circuit at 1 mA cm^{-2}, while in some cases (no additive, BDMPAC and CTAB) passivation is the termination cause at 10 mA cm^{-2}. TBAB shows the best performance at both c.d.s, while all other QASs cause an anticipated failure with respect to the additive-free electrolyte. TBAB slightly delays the termination by short circuit at 1 mA cm^{-2}, but it pushes the cell lifetime at 10 mA cm^{-2} beyond the maximum testing time of 256 h, chosen for this series of experiments. The peak of the volcano behaviour of the cycling response with respect to the JII, established on the basis of CV experiments (Cyclic voltammetry Subsection of the Results and Discussion Section and Figure 4), is confirmed by cycling experiments, that are less sensitive to the details of the QAS molecular structure with respect to intermediate-JII TBAB.

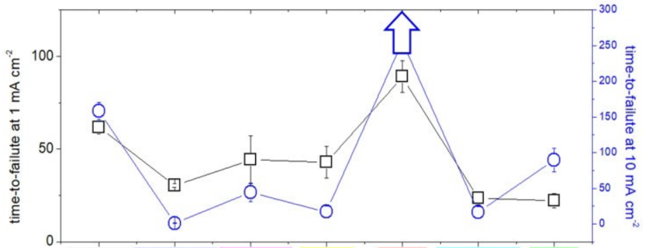

Figure 6. Time-to-failure derived from the data of Figure 5 and another replicated test run in the same conditions.

Regarding the behaviour of the different systems at 1 mA cm^{-2}, with the exception of the more electrochemically reactive BDMPAC, a regular potential response is found with a well-defined potential profile that can be described in terms of nucleation and growth of the cathodic Zn layer with different number densities of nuclei.[23] Mossy growth of Zn (see Imaging analysis of Zn shape change Subsection of the Results and Discussion Section) eventually leads to a short-circuit event, that in many cases is labile and, after some times, allows cell cycling to restart: we have neglected this aspect in this study and we have reported just two cases for reference (the DMDTDAB and PDADMAC traces in Figure 5A). In the present investigation we have assigned the cell-termination time in correspondence of the first short-circuit event occurring in the cell voltage time series. It is worth noting that TBAB exhibits a sort of running-in period with a higher cell voltage.

As hinted-at above, somehow counterintuitively, the cell lifetime is longer at 10 mA cm^{-2} (Figure 5B), with the exception of DMDTDAB which leads to short circuit after ca. one complete anodic-cathodic cycle: this particular experiment was replicated three times to verify this peculiar response. The longer lifetime at higher c.d. can be explained – as detailed below in the Imaging analysis of Zn shape change Subsection of the Results and Discussion Section (more specifically, Subsubsection Galvanostatic electrodeposition, investigated by stereomicroscopy) – with the fact that at low c.d. the mossy type of unstable Zn growth prevails and it is progressively reduced upon increasing the c.d. to an additive-dependent threshold for mossy growth suppression, of ca. $20 \div 30$ mA cm^{-2}. In a mossy-growth inhibition regime, with c.d.s that are still too low for dendrite development, passivation becomes the failure mode for the additive-free system. Following the volcano behaviour, low- (BDMPAC) and high-JII (CTAB) QASs show the same tendency of the additive-free system to fail by passivation, while intermediate-JII BPPEI, TBAB and PDADMAC suppress passivation, but only TBAB seems to enable suppression of short-circuit. Early failure by short-circuit might be due to a lowering of the threshold c.d. for dendrite development, but this point requires further study. Finally, one can note that, in analogy with the results obtained at 1 mA cm^{-2}, TBAB exhibits a running-in period in which the cell voltage increases, before reaching a constant value for a period that extends beyond our testing time.

Imaging analysis of Zn electrode shape change

This experiment aims to study the impact of QAS additives on the development of Zn electrode morphology, under a range of conditions that, on the one hand, could provide fundamental insight and, on the other hand, would be relevant for practical battery operation. This analysis consisted in the following steps: (i) additive screening under pure electrodeposition and cycling conditions (see below: Subsubsections Galvanostatic electrodeposition, investigated by stereomicroscopy and Galvanostatic cycling, investigated *post mortem* by SEM imaging); (ii) in-depth analysis – by *post mortem* stereomicroscopy and *in situ* XμCT – of the behaviour of the best-performing electrode, resulting from the screening step (see below: Subsubsections Galvanostatic electrodeposition, investigated by stereomicroscopy and Galvanostatic cycling, investigated by *in situ* XμCT).

Galvanostatic electrodeposition, investigated by stereomicroscopy – Initially, we carried out a simple screening test with all the QASs considered, Prolonged growth experiments (0.1 Ah cm^{-2}) were considered in a range of electrodeposition conditions relevant for practical galvanostatic charging of a battery with a Zn anode.

to rank the shape changes that could be assessed with a naked eye. In order to investigate worst-case conditions, we selected c.d.s in the mossy- and dendrite-growth ranges for the 2 M $ZnSO_4$ electrolyte without additives: 20 and 150 mA cm^{-2}, respectively. Subsequently, we focussed on the most promising additive, in view of in-depth imaging studies. It is worth noting that, to date, very simple, but enabling experiments of this type have not been reported in the literature for Zn in mildly acidic electrolytes. A simple schematic of the morphology classes obtained is shown in Figure 7. From this scheme it can be concluded that the growth morphologies at 20 mA cm^{-2} (mossy range) follow accurately the electrodeposition inhibition ranking (TBAB, PDADMAC and CTAB), while the results at 150 mA cm^{-2} (dendrite range) follow a different pattern, whereby the best additives for dendrite suppression are those lying in the low-to-intermediate electrodeposition inhibition range (DMDTDAB, BPPEI, BDMPAC and TBAB). Subsequent to the results at 20 mA cm^{-2}, TBAB, PDDMAC and CTAB were tested also at 1 mA cm^{-2} and were found to enable the growth of compact deposits also in this condition which is particularly critical for mossy Zn formation. The results of this visual screening test show that TBAB is the only additive showing both mossy and dendrite suppression activity. Moreover, TBAB exhibits a relatively low passivation inhibition (Eq. (2)) and lies in the intermediate JII range (Figure 4), showing a kind of volcano trend.

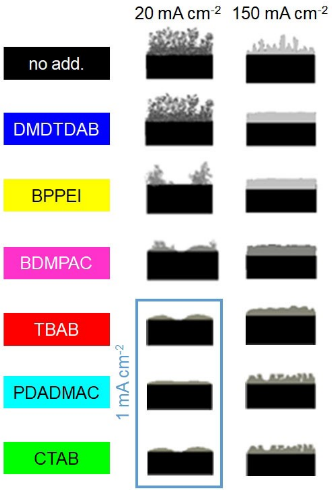

Figure 7. Morphology classes derived from galvanostatic deposition experiments (0.1 Ah cm^{-2}), obtained without and with QASs, arranged in the order of electrodeposition inhibition ranking (see Subsection Cyclic voltammetry of the Results and Discussion Section).

Morphological tests were completed by a systematic stereomicroscopic imaging analysis of galvanostatically grown Zn, as detailed in the previous paragraph, in the electrolyte containing TBAB, the QAS showing the best performance in terms of electrochemical behaviour (Subsections on Cyclic voltammetry and Galvanostatic cycling of coin cells in the Results and Discussion Section) and shape-change suppression in both the mossy and dendritic growth regimes.

In Figure 8 we show stereomicrographs of electrodeposits obtained in the absence and in the presence of TBAB at 10, 20, 50 and 200 mA cm^{-2}. In the additive-free electrolyte, at 10 mA cm^{-2} (Panels a, i, q) the deposit is fully mossy: 3D structures grow perpendicularly to the electrodes, which are well-adhered to the substrate, but mechanically weak and tend to break off. At 20 mA cm^{-2} a more compact layer grows (Panels b, j, r) in the first stages of electrodeposition, on top of which mossy, loose. Compact boulder-type structures, without any sign of dendritic formations grow at 50 mA cm^{-2} (Panels c, k, s): these deposits are shiny, uniform, compact and adherent. Finally, well-defined dendrites form at 200 mA cm^{-2} (Panels d, l, t). In brief, electrodeposition in the absence of additives confirms the commonly accepted literature vision of metal plating: as c.d. grows the metal morphology changes progressively from mossy to compact and finally to dendritic. In this context it is useful to underline that, since 50 mA cm^{-2} can be regarded as a reasonable upper bound for battery operation,[42] the formation of high-c.d. dendrites does not represent a serious threat, while the formation of mossy structures is possible basically in all the relevant charging conditions.

From Panels (e-h, m-p, u-x) of Figure 8, referring to the electrodeposits obtained from the TBAB solutions, it can be immediately noticed that, with the same c.d.s, much more compact shapes are obtained, confirming the suppression activity towards both mossy Zn (10 and 20 mA cm^{-2}) and Zn dendrites (200 mA cm^{-2}). All the stereomicrographs of deposits from TBAB-containing solutions show vertical patterns, that clearly correlate with electrolyte convection at the vertical cathodes, that is modified by the surfactant in a way that deserves deepening in future studies.

Galvanostatic cycling, investigated post mortem *by SEM imaging* – In order to gain understanding of the behaviour of Zn electrodes in real operating conditions, we carried out a series of cycling test in split cells, that reproduce exactly the conditions of the 2032 coin cells, the electrochemical performance of which has been described in the Subsection on Galvanostatic charge/discharge cycles of the Experimental Section, apart from the presence of the separator, which has been replaced with free electrolyte, in order to enable cell dismounting. With the aim to screen the effect of all additives, we have selected a single, critical electrochemical condition – 1 mA cm^{-2}, as severe mossy growth condition, as specified above in the previous Subsection – and to limit the impact of passivation on shape change, we have limited cycling to 14 hours. The electrochemical response is fully compatible with that reported in the Subsection on Galvanostatic charge/discharge cycles of the Experimental Section.

In Figure 9 we report SEM micrographs of the galvanostatically cycled Zn electrodes. All images show crystallites the morphology of which combines the features of electrodeposited Zn globules or filamentary mossy structures and ZnO platelets – that cover the globuli and the filamentary masses-, evidently resulting from the alternation of cathodic and anodic processes. Mossy structures are found in the absence of QAS and with the addition of DMDTDAB, BDMPAC and BPPEI, while the suppression of mossy growth and the stabilization of globular structures are found by adding TBAB, CTAB and PDMDMAC, confirming the results of Subsection on Galvanostatic electrodeposition, investigated by stereomicroscopy of the Results and Discussion Section, and showing a correlation with the JII. The type of additive, in correlation with mossy growth suppression, has a notable effect on the number density of crystallite clusters forming on the Zn electrodes (see bottom right Panel of Figure 9, blue plot). Again, TBAB, with an intermediate-to-high JII, is found to exhibit a better performance is terms of favouring a more homogeneous and compact morphology, corresponding to electrodeposition without excessive outgrowth and ZnO formation without excessive passivation. This cycling behaviour correlates with the higher

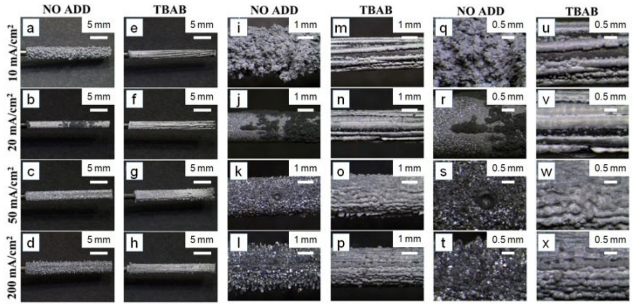

Figure 8. Steromicrographs of Zn electrodeposits obtained by galvanostatic deposition (0.1 Ah cm^{-2}) without and with added TBAB, at progressive magnifications.

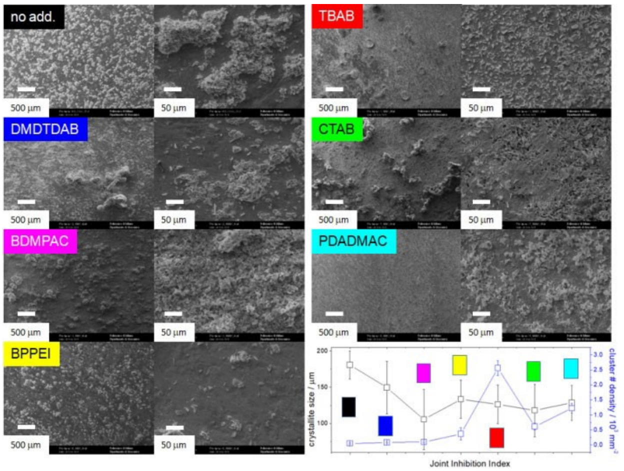

Figure 9. SEM micrographs of Zn electrodes cycled galvanostatically at 1 mA cm^{-2} in a split-cell.

nucleation rate highlighted in Subsection Cyclic voltammetry of the Results and Discussion Section.

Galvanostatic cycling, investigated by in situ *XμCT* – The method of election to follow the morphological evolution of metal during an electrochemical process is *in situ* XμCT, since this technique allows to obtain a 3D reconstruction of the metal deposit with a good spatial and contrast resolution in the intact reaction ambient and configuration. We resorted to this approach to gain in-depth understanding of the impact of TBAB, the single most prospective additive, on Zn cycling under representative battery conditions, in comparison with the additive-free case.

The selection and preparation of the samples was aimed at optimizing the operating time at the X-ray microtomographic station. We thus choose to compare the cycling behaviour of Zn electrodes at the two c. d. s enabled by the cell geometry described in the Subsection on X-ray computed tomography instrumentation and data analysis of the Experimental Section and in Section S2 of the Supporting Information, in the absence and in the presence of TBAB, which – on the basis of the outcomes of reported above (specifically: Subsections on Cyclic voltammetry and Galvanostatic cycling of coin cells and the previous two Subsubsections)-, resulted to be the best performing QAS out of the group considered. We thus built two identical cells for the tests with the two different electrolytes and worked with them in parallel. The first measurements were done with the two cells in pristine conditions and after two subsequent galvanostatic intervals of 2400 s at 10 and 25 mA cm^{-2} – corresponding to DODs of 30 and 15 %: both the c. d. s and the DOD are well into the range of practical interest[42] – for the external and internal electrodes, respectively. The last measurement was carried out after having held the same conditions for 4800 s, resulting in a doubling of the DODs. After each electrochemical run, the cell – under open-circuit conditions – was imaged by a XμCT scan the duration of which was of ca. 3 h. Overall, the electrochemical parameters employed would correspond to mild stress conditions for a practical reversible Zn cell.[42] The voltage/time curves applied for XμCT experiments are reported in Panel (B) of Figure 10. In line with the inhibiting effect of TBAB, the potentials are initially higher in the presence of the additive, but they progressively decrease with cycling time. This aspect, which was not clear from the cycling at lower c. d. studied in the Subsection on Galvanostatic cycling of coin cells, might point towards consumption or incorporation of the additive in the deposit and it will be the object of further investigation is future work. Moreover, it can be noticed that the voltage time series become progressively disturbed as cycling time lapses, precisely as a result of the electrode shape changes that will be described in the rest of the present Section. Finally, in line with the results of the above Subsection on Galvanostatic cycling of coin cells, we found that passivation is strongly mitigated by the application of higher c. d. s.

In Panel (A) of Figure 10 we report the 3D renderings of the cells in pristine conditions and after cycling in the absence and in the presence of TBAB. The slight morphological differences in the pristine state are due to the intrinsic variability of the electrodeposition process adopted for the growth of the Zn electrodes (see Section S2 of the Supporting Information for more details).

Referring to the outer electrode, operating at 10 mA cm^{-2}, from Panels (a)–(d) of Figures 10A, 11 and 12, it is possible to observe that, in the additive-free solution, mossy structures form and grow, coherently with the outcomes of the Subsubsection on Galvanostatic electrodeposition, investigated by stereomicroscopy. In addition, the porosity of the electrode tends to grow, as a result of uneven c. d. distribution possibly resulting from the formation of passivation patches, in line with the tendency highlighted in the Subsection on galvanostatic

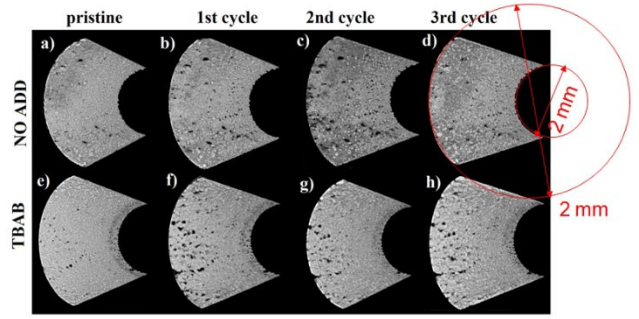

Figure 11. Results of *in situ* XμCT measurements: 3D rendering of a sub-VOI corresponding to a section of the outer Zn electrode (10 mA cm^{-2}) after subsequent cycling intervals.

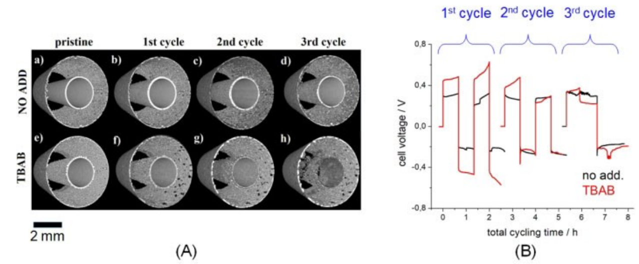

Figure 10. (A) Results of *in situ* XμCT measurements: 3D rendering of the same symmetric cell after subsequent cycling intervals. The images highlight the concentric Zn electrodes. The galvanostatic cycling was performed in 2 M $ZnSO_4$ electrolyte without (NO ADD) and with 0.1 g l^{-1} TBAB: inner electrode 25 mA cm^{-2}, outer electrode 10 mA cm^{-2}. (B) Cell voltage response upon galvanostatic cycling.

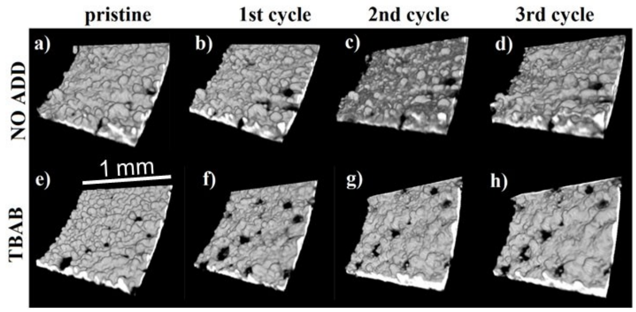

Figure 12. Details from Figure 11. Isosurface renderings showing representative regions of the electrolyte side of the outer Zn electrodes.

cycling of coin cells (Figure 5B). Finally, the thickness of the Zn electrode progressively decreases with the number of cycles: this process corresponds to anode unbalancing and capacity fade, and is due to the formation of dead metal, caused by the detachment of mossy structures, and insoluble ZnO precipitates in the bulk of the electrolyte.

The addition of TBAB gives rise to an appreciable reduction of mossy growth onto the outer Zn electrode, that appears more compact and smoother, coherently with the coin-cell cycling results of the Subsection on Galvanostatic cycling of coin cells (Figure 5B).

In the experiment carried out in the absence of additive, the morphology evolution of the inner rod, operating at 25 mA cm^{-2}, during the first two cycles (Panels (a)–(c) of Figures 10A, 13 and 14) indicates progressive coarsening, with the formation on the whole surface of compact, 3D structures with a thin base; in addition, a few isolated dendrites can be noticed. This behaviour is coherent with the fact that at this c. d. the dendrite formation threshold is approached. A characteristic feature of the inner Zn electrode cycled in the additive-free electrolyte is that, in some areas, a crust is found to form, which covers the original deposit leaving a cavity between the two (Figure 14B). After the third cycle in the additive-free case (Panels (d) of Figures 10A, 13 and 14), the deposit is ca. 30% thinner than the original one and dead Zn particles form, close to the electrode surface, but detached from it (see, in particular, Figure Panel (c) of Figure 14A).

In the experiment carried out with TBAB, after the first cycle the roughness of the inner electrode increases more markedly than in the absence of the additive (Panels (e)-(f) of Figures 10A, 13 and 14). After the second cycle, the deposit appears profoundly modified and the surface is covered with large 3D structures with a thin base (Panels (g) of Figures 10A, 13 and 14). Moreover, after the third cycle extensive formation of dead Zn can be noticed. The drop in potential observed about 0.5 h after the beginning of the third cycle might be due to the notable metal outgrowth. It is worth noting that poorer performance of the Zn electrode in the presence of TBAB upon cycling at higher c. d. s is coherent with our results of the Subsection on Galvanostatic cycling of coin cells and is in keeping with the behaviour of this additive in alkaline ambient.[23] In the present case, worse behaviour at 25 mA cm^{-2} with the TBAB-containing electrolyte might be due to a lowering of the c. d. for dendrite inception, that might correlate with the early failure of coin cells by short-circuit at 10 mA cm^{-2}, as found in the presence of DMDTDAB, BPPEI and PDADMAC.

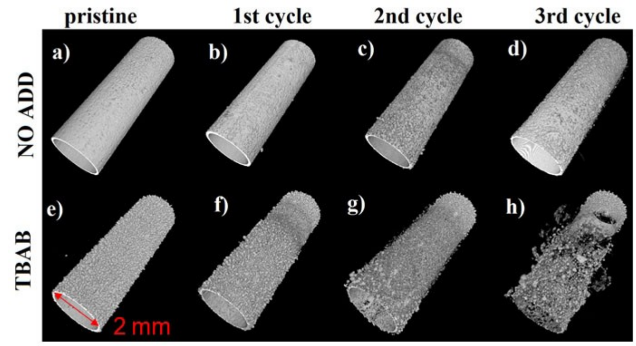

Figure 13. Results of *in situ* XµCT measurements: 3D renderings of the inner Zn electrode (25 mA cm^{-2}) after subsequent cycling intervals.

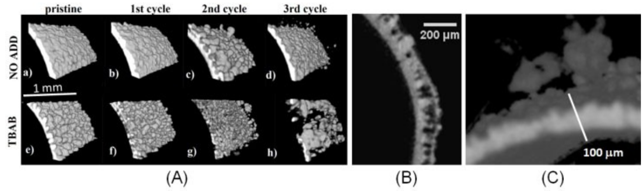

Figure 14. Zoomed regions from Figure 13. (A) Isosurface renderings showing representative regions of the electrolyte side of the internal Zn electrodes. (B) Detail of an axial slice of the inner Zn electrode showing a region of the internal electrode for the additive-free electrolyte sample after the 2nd cycle. (C) 3D rendering showing a detail of the inner electrode: additive-free electrolyte, after 3rd cycle.

Conclusion

This work focuses on the electrochemical behaviour of Zn foils in mildly acidic aqueous electrolytes, it is aimed at gaining insight into the cycling behaviour of Zn anodes for electrically rechargeable batteries. Specifically, the role of quaternary ammonium salts (QASs) as additives has been studied systematically, by a combination of electrochemical measurements and *post mortem* as well as *in situ* multi-scale and multi-modal imaging analyses. The literature in the field, at the time of this writing, is scanty and scattered. Methodologically, this study has been developed against the background of cognate studies in alkaline environment, which is extensively documented, though perhaps not as systematically as one would wish.

A general result, which is compatible with scattered literature results, but has been systematized in this work, is that compact and uniform Zn electrodeposits can be obtained from 2 M $ZnSO_4$ solutions in a specific current density (c. d.) range, the limits of which depend on the specific QAS considered. Above the upper c. d. limit, dendrites tend to form, essentially under diffusion control. In neutral electrolytes, such upper c. d. limit was found to be above the range presently considered for battery recharge: this finding in principle points out the possibility of increasing the recharge rate of secondary batteries with Zn anodes. It is worth noting that since the concentrations of Zn ions currently proposed for neutral electrolytes are 4 to 20 times higher than those used in alkaline solutions, the former class of electrolytes intrinsically enables lower mass-transport limitations. Below the lower c. d. limit, instead, non-compact, mossy structures form: this lower limit is not appreciably different in neutral and alkaline electrolytes. Since mossy structures were found to grow even below 20 mA cm^{-2}, the suppression of these structures is currently more practically urgent than that of high-c. d. dendrites.

In analogy with our recent results regarding the alkaline system,[21,23] in this paper we highlighted that the synergy between the cathodic and the anodic behaviour of Zn – its passivation behaviour, in particular – for a given combination of electrolyte and c.d., is of fundamental importance for the stabilization of anode morphology during extended cycling. Moreover, combining the results of this work and those of a recent study of ours, based on X-ray absorption microspectroscopy,[22] we could pinpoint that, in mildly acidic ambient, passivation is favoured by the local cathodic alkalinisation, linked to HER running concomitantly with Zn plating under strong cathodic polarization.

Regarding the effect of QAS additives, systematic cyclic voltammetry (CV) investigations highlighted that these species inhibit – to different extents and in a molecule-specific way – both the cathodic and the anodic reactions. The increment of cathodic overpotential can be associated to a kinetic inhibition of the deposition reaction due, on the one hand, to the cathodic adsorption of QAS, and, on the other hand, to the formation of passivating layers as a result of holding in the preceding anodic intervals. Cathodic inhibition effectiveness, as assessed by CV, was confirmed by galvanostatic electrodeposition experiments, showing that three additives exhibiting the highest cathodic inhibition index (TBAB < PDADMAC < CTAB) allowed a complete suppression of mossy structures for c. d. s < 20 $\mathrm{mA\,cm^{-2}}$, while at higher c. d. s irregular deposits were obtained. The anodic and cathodic inhibition effectiveness can be ranked with a joint inhibition index (JII), according to which DMDTDAB < BPMPAC < BPPEI < TBAB < PDADMAC < CTAB. Intermediate JII values correlate with better performance and shape-change suppression under cycling conditions.

Discharge-charge cycling tests in CR2032 coin-cells and split-cells of the same geometry, allowed to assess the ability of TBAB in the suppression of mossy deposits under realistic battery operating conditions (range 10 ÷ 25 $\mathrm{mA\,cm^{-2}}$). *Post mortem* scanning electron microscopy (SEM) inspection of electrodes cycled in a split-cell unveiled that the morphology obtained in presence of TBAB were smooth and uniform. With the exception of PDADMAC, that enables smooth deposits for limited cycling times, the other additives gave rise to deposit morphologies that are similar, or even more irregular, than the ones obtained without additive.

The optimal QAS TBAB was thus selected for *in situ* 3D X-ray imaging of symmetric cells, that was carried out in electrolytes without and with added TBAB, at c. d. s below (10 $\mathrm{mA\,cm^{-2}}$) and above (25 $\mathrm{mA\,cm^{-2}}$) the mossy-deposit threshold. The markedly beneficial effect of TBAB in the lower-c. d. range was confirmed, while – in its presence – worse shape changes, with formation of large amounts of dead metal were observed than in its absence. A similar behaviour was found in alkaline ambient.[23]

This study, based on complementary electrochemical and 2D/3D imaging techniques, provides a methodological path, that can be naturally extended to systematic device-scale and *in operando* microspectroscopic testing. Accompanied by systematic quantitative evaluation of the electrical device response (see, e. g.[23]), this approach would enable a knowledge-based development of material modifications and cycling protocols, in view of better cyclability of Zn anodes, towards full-battery scale implementation.

Experimental Section

This experimental work is centered on electrochemical measurements (cyclic voltammetry, chronopotentiometry and galvanostatic-cycling in split-cells) and imaging characterization: *ex situ* by stereomicroscopy and scanning electron microscopy (SEM) and *in situ* by X-ray computed microtomography (XμCT). The investigation revolves around the effect of a series of QASs on the combined cathodic and anodic evolution of Zn anodes in mildly acidic $ZnSO_4$ aqueous electrolyte.

Materials

In the electrochemical measurements were carried out in mildly acidic aqueous $ZnSO_4$ electrolytes. For cyclic voltammetry measurements, electrolyte consisted of supporting electrolyte – an aqueous solution of 0.5 M Na_2SO_4 (Sigma-Aldrich) as supporting electrolyte-, to which 10 mM $ZnSO_4$ (Sigma-Aldrich) (pH 5.5) and QAS were added (0.1 $\mathrm{g\,l^{-1}}$ of each QAS, except BPPEI, that was employed in 0.01 $\mathrm{g\,l^{-1}}$ concentration), according to the experimental requirements, detailed where relevant. For our CV measurements, a low concentration of $ZnSO_4$ was selected for electroanalytical purposes, in order to enable mass-transport controlled voltammetric cathodic features and a well-defined stripping peak, that would be offset by the high limiting current density and the large amount of deposited Zn, corresponding to the full battery concentration. For galvanostatic deposition, stripping and charge/discharge cycling, the electrolyte was an aqueous solution of 2 M $ZnSO_4$ (Sigma-Aldrich) (pH 3.6). Milli-Q water without and with the above-mentioned amounts of additives. In addition to QAS, we also tested 0.1 M $MnSO_4$ as additive (pH 3.4), to simulate a common ZIB electrolyte: information on this system is reported in Section S3 of the Supporting Information.

Quaternary ammonium salts (QAS) are cationic surfactants, widely employed as additives in metal plating. QASs have a quaternary ammonium cation, which is a nitrogen atom, bonded to four alkyl groups and hence hosts a single positive charge. QAS are stable toward most of bases and acids and highly soluble in water. Under high cathodic polarization they can degrade through an irreversible reduction reaction, producing an amine and a hydrocarbon.[43] No information can be found in the literature about the electrochemical oxidation of these compounds. QASs are generally biodegradable and, even if they are generally toxic for aquatic organisms,[44] they typically do not represent an environmental issue in the really small amounts required for battery applications. The use of QASs to improve electrodeposits quality is well established, but their working mechanisms are poorly understood. QAS adsorption on the Zn cathode is generally taken for granted: blockage of favourable deposition sites, tip growth inhibition[45] and increased nucleation rate[46] are their commonly reported mechanism. QASs are also a class of additives strictly associated to the ion-paring mechanism,[47] since this mechanism is effective only for negatively-charged depositing ions, such as zincate ions in alkaline environment, one can predict differences in the behaviour of these additives between alkaline and mildly acidic electrolytes. The effect of QASs on the electrodeposit morphology depends strongly on the nature of the alkyl groups; for aliphatic QASs the cathodic inhibition and the ability to suppress dendrites seems to correlate positively with the chain length.[48,49] Bulkier alkyl groups delocalize the positive charge of the nitrogen on the whole molecule, decreasing the cation polarity as well as, presumably, the strength of its adsorption on the cathode. Long aliphatic chains, of course, also decrease the QAS solubility. QASs have also been studied as corrosion inhibitors for steel[50] and primary Zn batteries:[51,52] the possible double effect as levellers and corrosion inhibitors–

pinpointed for alkaline conditions in[21,23]–makes them particularly attractive for the application in mildly acidic battery electrolytes.

In this study, different QAS were considered (see Figure 1), following the approach we took in,[21] were we investigated them in alkaline electrolytes for Zn batteries. Tetra-butyl ammonium bromide (TBAB) is a QAS with four identical four carbon aliphatic chains. Similar cations–with two, three, and five carbon atoms in the aliphatic chains–were studied in chloride electrolyte.[48] Hexadecyl (or cetyl) tri-methyl ammonium bromide (CTAB) differs from TBAB mainly for its long 12 carbon atoms aliphatic chain, TBAB and CTAB are two of the most common QAS employed in the metal-plating literature. Di-methyl di-tetradecyl ammonium bromide (DMDTDAB) has 2 long aliphatic chains which makes it more insoluble than CTAB, so that, at the concentrations commonly adopted for the other additives, it is present mainly as a micelle rather than as a free molecule:[53] Apart from,[21] no other investigations are known in which DMDTDAB was adopted as an electrodeposition additive. Benzyl dimethyl phenyl ammonium chloride (BDMPAC), exhibiting with two aromatic functionalities, is an additive employed in gold plating from near-neutral solutions and it exhibits a notable stabilizing activity in the replacement of alkaline with near-neutral pH.[40] Benzyl-phenyl modified polyethyleneimine (BPPEI) is a polymeric QAS with the same functionalities of BDMPAC, this compound is interesting because it is a QAS but has the structure of PEI, which is also an additive studied for ZIB anodes: this additive has been successfully used as dendrite suppressor in acidic Cu plating.[38] Poly di-allyl di-methyl ammonium chloride (PDADMAC) is a polymer in which the tetravalent nitrogen is included in a five-atoms ring, was adopted as component for an artificial SEI in metallic lithium batteries, that might interact with the corrosion products, giving rise to a stable, ionically conducting anodic film.

Electrochemical measurements

The effect of QASs was investigated with three types of electrochemical measurements: (i) Cyclic voltammetry (CV); (ii) galvanostatic and stripping deposition on graphite amd Zn substrates at different c.d.s; (iii) symmetric cell cycling at different c.d.s in symmetric split-cells and in a cyclindrical cell, specifically designed for three-dimensional (3D) X-ray imaging analysis. Specifically, the two most performing additives (TBAB and PDADMAC) were identified on the basis of CV and galvanostatic experiments, and they were investigated with galvanostatic deposition and stripping tests on a Zn substrate. After these tests, the study of TBAB, which resulted to be the most effective QAS, was deepened through *in situ* tomography during galvanostatic cycling. All electrochemical measurements were carried out with a 3F VersaSTAT potentiostat/galvanostat. The reference electrode (RE) was an Ag/AgCl 3 M KCl (AMEL 373/SSG/12) and all potentials are referenced to this scale.

Cyclic voltammetry (CV) – The CV protocol was based on that described in,[22] and modified in view of the addition of organics. CVs were performed in a standard three-electrode cell (AMEL 497 Universal Cell), with two identical platinum counter electrodes (CE: AMEL 805/SPG/12: 1 mm diameter, 5 mm long), placed symmetrically with respect to the working electrode (WE) and RE to improve the uniformity of the current distribution and reduce ohmic losses. A glassy carbon (GC) electrode (AMEL 492/GC/3) with a surface area of 0.07 cm^2 was employed as WE. GC was chosen to obtain better resolved information regarding the impact of the QASs on Zn nucleation, thanks to the high nucleation overvoltage of this material. The cell contained 30 ml of electrolyte (see the previous Subsection for the composition), which was degassed by N_2 bubbling (0.5 nlt/min) before running the experiment and kept under a blanket of flowing N_2 during the electrochemical measurements. CVs were performed at 25 $mV\,s^{-1}$, in relevant potential ranges that will be specified. All CV measurements were repeated three times, in order to assess the reproducibility of the system. Specifically, before each experiment, the electrode was immersed in 70% nitric acid for a few seconds, rinsed with DI water, polished with 2500 grinding paper and finally sonicated for 5 min in DI water. To ensure complete removal of zinc compounds and organics, the Pt CEs, the salt bridge of the RE and all the cell components were washed with 70% nitric acid and accurately rinsed with DI and Milli-Q water. All components and electrodes were finally rinsed with Milli-Q water. The CVs were performed with the following protocol: (i) The cleaned GC electrode was subjected to CV cycling (5 cycles in range $0.5 \div -1.8$ V, starting from the open-circuit potential (OCP)) in the pure supporting electrolyte (see the previous Subsection) to positively assess the WE condition. (ii) $ZnSO_4$ was added to the electrolyte, then a second CV was performed: 10 cycles from -0.5 to -1.6 V, starting from anodic terminal potential. (iii) 1 ml of concentrated additive solution was introduced into the cell, in order to achieve the desired concentration. The solution was degassed again as before, and a third CV was performed, with the same parameters of the second one.

Galvanostatic electrodeposition – Galvanostatic polarization can be regarded as the simplest type of electrochemical operating condition imposed to the Zn electrode of a battery. We employed cathodic tests for a screening of the effect of QASs on morphology development during charge. Galvanostatic deposition was performed in two-electrode configuration in cylindrical glass cells hosting 5 ml of electrolyte, equipped with a Zn tube (5 mm diameter, 250 um thickness) as the anode and a graphite cylindric rod (2 mm diameter) as the cathode. The electrolyte was 2 M $ZnSO_4$, to which the various additives were introduced, mentioned in the previous Subsection. The graphite rod cathodes were pretreated by immersion in 70% nitric acid and then accurately rinsed with DI and Milli-Q water. The Zn electrodes were degreased with acetone and rinsed with DI and Milli-Q water prior to each test. The cell body washed with 70% nitric acid and accurately rinsed with DI and Milli-Q water. Galvanostatic deposition was performed at 1, 10, 20, 50 and 200 $mA\,cm^{-2}$, depositing nominally 0.1 $Ah\,cm^{-2}$ of Zn. After the deposition, the samples were washed gently with Milli-Q water and dried in a N_2 flow.

Galvanostatic charge/discharge cycles (GCD) – These measurements were carried out in CR2032 coin cells. The electrodes were fabricated by punching 250 μm thick Zn foil (99.98% Alfa Aesar, cleaned as described in the previous Subsubsection) into a 12 mm diameter disks. The electrodes were put in contact with two austenitic stainless steel (AISI 304) current collectors (12 mm diameter, 150 μm thick). A 260 μm thick glass microfiber foil (Whatman) was punched into a 19 mm disk and used as the separator, soaked with 350 μl of electrolyte. The assembly schematic of the coin-cells is shown in Figure S6 of the Supporting Information. The electrolyte was 2 M $ZnSO_4$ without and with added QAS, as indicated in the previous Subsection. GCD cycles were performed at 1 and 10 $mA\,cm^{-2}$ with 60 min periods (30 min positive and 30 min negative current), corresponding to 0.5 and 5 $mAh\,cm^{-2}$. We selected these depths of discharge (DOD) to be in line with the literature on GCD of ZIBs (see detailed discussion on this point in[23]), but it is worth noting that this is lower than that of practical battery operation.[42] The cycling adopted for *in situ* XμCT experiments (described in the previous two Subsubsections) is instead performed to DODs that are fully representative of concrete working conditions. Each GCD cycle was run until the cell potential reached a cut-off of ± 1 V, corresponding to experiment termination by passivation. Following the approach of,[23] the measurements were replicated twice, in order to gain quantitative insight into the evolution of the potential profiles and times-to-failure of the cells.

In order to study the shape changes of Zn electrodes, we carried out SEM imaging after galvanostatic cycling under in a split-cell, reproducing the geometry of 2032 coin cells. The split cell was an EL-CELL ECC-AIR-NI, the electrodes consisted of two Zn discs as above. At variance with the coin-cell experiments, in the split-cell, the electrodes were kept separated by an O-ring and the cell was filled with 300 μl of electrolyte. As detailed in,[23] using a free electrolyte instead of one soaked into a separator is necessary to be able to open the cell after cycling without damaing the Zn and ZnO patterns resulting from shape change. Of course cycling without and with a separator yields different electrochemical responses and types of shape change, that have been insufficiently studied so far and warrant more insightful investigation in future work. In any case the aim here is it to gain understanding of the impact of QAS additives on shape changes in coin-cell context under cycling, and this system is appropriate. After completion of the measurement, representative cells were disassembled and the two Zn discs were washed gently with DI water, dried with N_2, and collected for SEM imaging.

X-ray computed microtomography (XμCT): instrumentation and data analysis – XμCT measurements were performed by using the TomoLab station available at Elettra synchrotron facility (Basovizza, Trieste, Italy).[54–56] This instrument is equipped with a sealed microfocus X-ray source (Hamamatsu L9181, Japan) delivering a polychromatic beam in the Voltage range of 40–130 kV with a maximum power of 39 W and a minimum focal spot of 5 μm. A 12-bit, 4008×2672 pixels, water-cooled CCD camera (XDI-VHR, Photonic Science, UK), coupled to a fiber optic taper to a Gadox scintillator screen, was used to record the sample (electrochemical cell) radiographs (projections) at different angular views.[57] In this open and flexible system, exploiting the magnification effect offered by the cone-beam geometry, the source-to-sample (SSD) and source-to-detector (SDD) distances can be varied in order to achieve a spatial resolution close to the focal spot size of the source working both in absorption and propagation-based phase-contrast modes.[58] A 2×2 binning has been applied to the CCD camera pixels, resulting in an effective pixel size of 5.0 μm. In our measurements we set the following experimental conditions: Voltage = 130 kV, power = 8 W, SSD = 80 mm, SDD = 400 mm, exposure time per projection = 5.8 s. From the 1800 projections acquired during a 360° rotation of the sample, a set of 2D slices was reconstructed with the open source software Nrecon 1.7 (Bruker, USA) based on the FDK algorithm.[59] The same software has been used to reduce/remove beam hardening and ring artefacts in the reconstructed slices. After tomographic reconstruction, the raw data collected in each scan generated 1270 axial slices that were stacked and converted to 8-bit .raw format files (virtual volumes) with the Fiji software.[60] This software was also used to select and crop sub-volumes of interest (sub-VOI) to isolate the deposits on the external surface of the inner rod electrode and the internal surface of the external hollow-cylinder electrode. *In situ* capability was obtained by imaging the same region of the cell – thanks to appropriate 3D registration – after representative cycling intervals.

Fabrication of a customized electrochemical cell for in situ *XμCT characterization* – A cylindrical electrochemical cell, optimized for *in situ* XμCT imaging during Zn electrode cycling, has been designed and developed for this particular study. The cell body consisted of a graphite tube, with a wall thickness of 1 mm, an internal diameter of 5 mm and a height of 20 mm. The portion of the internal surface of the cell body, filled with the electrolyte works as one of the electrodes. The second electrode was a graphite rod, 2 mm in diameter, fixed along the axis of the cell body with plastic centring supports. The cell is mounted on a copper cylinder, that also provides electrical contact to the cell body, into which a threaded PVC connector is screwed, providing the mechanical connection to the rotation stage of the TomoLab station. In order to use this cell as a Zn/Zn symmetric cell, 100 ± 10 μm thick Zn layers were electrodeposited onto the internal graphite surface of the cell body and the graphite rod. More details on the cell geometry, fabrication, electrochemical calibration data and operating conditions are reported in Section S2 of the Supporting Information. The cylindrical electrode geometry, exploited for symmetric cell work, offers one degree of freedom in the c.d.s that can be applied to the internal and external electrodes in galvanostatic operation, allowing to test two cycling c.d.s in a single imaging experiment. In the case implemented in this work, the electrode area ratio is 2.5.

Stereomicroscopy and Scanning Electron Microscopy – The stereomicroscopy analyses were performed using a Leica ® M165C stereomicroscope. Samples were observed at three magnification levels (5×-20×-40×) in order to highlight the deposit morphologies as a whole and also in detail in specific areas.

The SEM analyses were conducted with a Zeiss model EVO 50 SEM, equipped with an energy dispersive spectroscopy (EDS) probe Oxford model INCA Energy 200. The voltage was set to 20 kV, the filament and beam current were set to 2.7 A and 78 μA respectively. Finally, the probe current was set between 80 pA and 100 pA.

Conflict of Interest

The authors declare no conflict of interest.

Data Availability Statement

The data that support the findings of this study are available from the corresponding author upon reasonable request.

Keywords: batteries · mildly acidic · quaternary ammonium salts · X-ray microtomography · zinc

[1] X. Yu, A. Manthiram, *Adv. Energy Sustain. Res.* **2021**, *2*, 2000102.
[2] E. J. Berg, C. Villevieille, D. Streich, S. Trabesinger, P. Novákz, *J. Electrochem. Soc.* **2015**, *162*, A2468–A2475.
[3] Y. Li, J. Yang, J. Song, *Renewable Sustainable Energy Rev.* **2017**, *74*, 19–25.
[4] G. Zhao, X. Wang, M. Negnevitsky, *iScience* **2022**, *25*, 103744.
[5] B. Diouf, R. Pode, *Renewable Energy* **2015**, *76*, 375–380.
[6] J. Galos, K. Pattarakunnan, A. S. Best, I. L. Kyratzis, C.-H. Wang, A. P. Mouritz, *Adv. Mater. Technol.* **2021**, *6*, 2001059.
[7] Y. Chen, Y. Kang, Y. Zhao, L. Wang, J. Liu, Y. Li, Z. Liang, X. He, X. Li, N. Tavajohi, B. Li, *J. Energy Chem.* **2021**, *59*, 83–99.
[8] K. Liu, Y. Liu, D. Lin, A. Pei, Y. Cui, *Sci. Adv.* **2018**, *4*, eaas9820.
[9] M. Dürr, A. Cruden, S. Gair, J. R. McDonald, *J. Power Sources* **2006**, *161*, 1400–1411.
[10] J. Yang, C. Hu, H. Wang, K. Yang, J. B. Liu, H. Yan, *Int. J. Energy Res.* **2016**, *41*, 336–352.
[11] Y. Li, J. Fu, C. Zhong, T. Wu, Z. Chen, W. Hu, K. Amine, J. Lu, *Adv. Energy Mater.* **2019**, *9*, 1802605.
[12] A. R. Mainar, L. C. Colmenares, J. A. Blázquez, I. Urdampilleta, *Int. J. Energy Res.* **2018**, *42*, 903–918.
[13] Y. Liu, X. Lu, F. Lai, T. Liu, P. R. Shearing, I. P. Parkin, G. He, D. J. L. Brett, *Joule* **2021**, *5*, 2845–2903.
[14] J. Yan, J. Wang, H. Liu, Z. Bakenov, D. Gosselink, P. Chen, *J. Power Sources* **2012**, *216*, 222–226.
[15] N. Yesi, J. Long, B. Li, X. Li, S. Zhang, F. Yang, X. Zeng, Z. Yang, W. K. Pang, Bolati, N. Umirov, A. Koishybay, M. Omarova, I. Kurmanbayeva, Y. Zhang, Y. Zhao, Z. Bakenov, *Electrochim. Acta* **2015**, *152*, 505–511.

[16] J. Hao, Z. Guo, *Adv. Funct. Mater.* **2019**, *29*, 1903605.
[17] A. R. Mainar, E. Iruin, J. A. Blázquez, *Energy Technol.* **2020**, *8*, 2000476.
[18] P. He, J.-L. Liu, W.-J. Cui, J.-Y. Luo, Y.-Y. Xia, *Electrochim. Acta* **2011**, *56*, 2351–2357.
[19] H. Jia, Z. Wang, B. Tawiah, Y. Wang, C.-Y. Chan, B. Fei, F. Pan, *Nano Energy* **2020**, *70*, 104523.
[20] Z. Xing, C. Huang, Z. Hu, *Coord. Chem. Rev.* **2022**, *452*, 214299.
[21] F. Rossi, C. Mele, M. Boniardi, B. Bozzini, *ChemElectroChem* **2020**, *7*, 1752–1764.
[22] M. Kazemian, F. Rossi, A. Casaroli, T. Caielli, B. Kaulich, M. Kiskinova, I. Sgura, B. Bozzini, *J. Power Sources* **2022**, *524*, 231063.
[23] F. Rossi, L. Mancini, I. Sgura, M. Boniardi, A. Casaroli, A. P. Kao, B. Bozzini, *ChemElectroChem* **2022**, *9*, e202101537.
[24] F. Gao, B. Mei, X. Xu, J. Ren, D. Zhao, Z. Zhang, Z. Wang, Y. Wu, X. Liu, Y. Zhang, *Chem. Eng. J.* **2022**, *448*, 137742.
[25] X. Ma, X. Cao, M. Yao, L. Shan, X. Shi, G. Fang, A. Pan, B. Lu, J. Zhou, S. Liang, *Adv. Mater.* **2022**, *34*, 2105452.
[26] S. Clark, A. R. Mainar, E. Iruin, L. C. Colmenares, J. Alberto Blázquez, J. R. Tolchard, A. Latz, B. Horstmann, *J. Mater. Chem. A* **2019**, *7*, 11387–11399.
[27] E. Iruin, A. R. Mainar, M. Enterría, N. Ortiz-Vitoriano, J. Alberto Blázquez, L. C. Colmenares, T. Rojo, S. Clark, B. Horstmann, *Electrochim. Acta* **2019**, *320*, 134557.
[28] C. Wang, J. Li, Z. Zhou, Y. Pan, Z. Yu, Z. Pei, S. Zhao, L. Wie, Y. Chen, *EnergyChem* **2021**, *3*, 100055.
[29] W.-F. Wu, X. Yan, Y. Zhan, *Chem. Eng. J.* **2023**, *451*, 138608.
[30] S. Inoguchi, A. Kitada, K. Fukami, K. Murase, *J. Electrochem. Soc.* **2020**, *167*, 162511.
[31] A. Clarisza, H. K. Bezabh, S.-K. Jiang, C.-J. Huang, B. W. Olbasa, S.-H. Wu, W.-N. Su, B. J. Hwang, *ACS Appl. Mater. Interfaces* **2022**, *32*, 36644–36655.
[32] D. P. Trudgeon, K. Qiu, X. Li, T. Mallick, O. O. Taiwo, B. Chakrabarti, V. Yufit, N. P. Brandon, D. Crevillen-Garcia, A. Shah, *J. Power Sources* **2019**, *412*, 44–54.
[33] R. K. Ghavami, Z. Rafiei, *J. Power Sources* **2006**, *162*, 893–899.
[34] M. Shimizu, K. Hirahara, Y. Ishida, S. Arai, *J. Electrochem. Soc.* **2019**, *166*, A2242.
[35] M. Shimizu, K. Hirahara, S. Arai, *Phys. Chem. Chem. Phys.* **2019**, *21*, 7045–7052.
[36] G. D. Wilcox, P. J. Mitchell, *J. Power Sources* **1990**, *32*, 31–41.
[37] S. J. Banik, R. Akolkar, *Electrochim. Acta* **2015**, *179*, 475–481.
[38] B. Bozzini, L. D'Urzo, C. Mele, *Electrochim. Acta* **2007**, *52*, 4767–4777.
[39] A. Fanigliulo, B. Bozzini, *Electrochim. Acta* **2002**, *47*, 4511–4521.
[40] A. Fanigliulo, B. Bozzini, *J. Electroanal. Chem.* **2002**, *530*, 53–62.
[41] M. D. Tikekar, S. Chiudhury, Z. Tu, L. A. Archer, *Nat. Energy* **2016**, *1*, 16114.
[42] J. F. Parker, J. S. Ko, D. R. Rolison, J. W. Long, *Joule* **2018**, *2*, 2519–2527.
[43] S. D. Ross, M. Finkelstein, R. C. Petersen, *J. Am. Chem. Soc.* **1960**, *82*, 1582–1585.
[44] C. Zhang, F. Cui, G.-M. Zeng, M. Jiang, Z.-Z. Yang, Z.-G. Yu, M.-Y. Zhu, L.-Q. Shen, *Sci. Total Environ.* **2015**, *518–519*, 352–362.
[45] A. Bayaguud, X. Luo, Y. Fu, C. Zhu, *ACS Energy Lett.* **2020**, *5*, 3012–3020.
[46] J. Bressan, R. Wiart, *J. Appl. Electrochem.* **1979**, *9*, 43–53.
[47] T. C. Franklin, *Surf. Coat. Technol.* **1987**, *30*, 415–428.
[48] D. J. Mackinnon, J. M. Brannen, *J. Appl. Electrochem.* **1982**, *12*, 21–31.
[49] C. J. Lan, C. Y. Lee, T. S. Chin, *Electrochim. Acta* **2007**, *52*, 5407–5416.
[50] R. Fuchs-Godec, *Colloids Surf.* **2006**, *280*, 130–139.
[51] D. Zang, L. Li, *Corros. Sci.* **2001**, *43*, 1627–1636.
[52] J. Zhu, Y. Zhou, C. Gao, *J. Power Sources* **1998**, *72*, 231–235.
[53] A. G. Diress, M. M. Yassine, C. A. Lucy, *Electrophoresis* **2007**, *8*, 1189–1196.
[54] B. Bozzini, A. Gianoncelli, C. Mele, A. Siciliano, L. Mancini, *J. Archaeol. Sci.* **2014**, *52*, 24–30.
[55] L. Mancini, D. Dreossi, C. Fava, N. Sodini, G. Tromba, S. Faretto, F. Montanari, *TOMOLAB, The new X-ray microtomography facility @ ELETTRA, Elettra Highlights* **2007**, *6*, 128–129.
[56] M. Polacci, D. R. Baker, L. Mancini, S. Favretto, R. J. Hill, *J. Geophys. Res.* **2009**, *114*, B01206.
[57] C. Kak, M. Slaney, *IEEE*, IEEE Press New York, **1987**, pp. 113–134.
[58] S. V. Wilkins, T. E. Gureyev, D. Gao, A. Pogany, A. W. Stevenson, *Nature* **1996**, *384*, 335–338.
[59] L. A. Feldkamp, L. C. Davis, J. W. Kress, *J. Opt. Soc. Am.* **1984**, *1*, 612–619.
[60] J. Schindelin, I. Arganda-Carreras, E. Frise, V. Kaynig, M. Longair, T. Pietzsch, S. Preibisch, C. Rueden, S. Saalfeld, B. Schmid, J.-Y. Tinevez, D.-J. White, V. Hartenstein, K. Eliceiri, P. Tomancak, A. Cardona, *Nat. Methods* **2012**, *9*, 676–682.

Manuscript received: December 2, 2022
Revised manuscript received: January 13, 2023
Version of record online: February 2, 2023